PAPER

A two-compartment bone tumor model to investigate interactions between healthy and tumor cells

To cite this article: Aylin Komez *et al* 2020 *Biomed. Mater.* **15** 035007

Biomedical Materials

PAPER

A two-compartment bone tumor model to investigate interactions between healthy and tumor cells

RECEIVED
26 November 2019

REVISED
8 January 2020

ACCEPTED FOR PUBLICATION
14 January 2020

PUBLISHED
5 March 2020

Aylin Komez[1,2], **Arda Buyuksungur**[2], **Ezgi Antmen**[2], **Wojciech Swieszkowski**[3], **Nesrin Hasirci**[1,2,4,5] and **Vasif Hasirci**[1,2,6,7]

[1] Graduate Department of Biotechnology, Middle East Technical University (METU), Ankara, 06800, Turkey
[2] BIOMATEN, METU Center of Excellence in Biomaterials and Tissue Engineering, Ankara, 06800, Turkey
[3] Faculty of Materials Science and Engineering, Warsaw University of Technology, Warsaw, 02 507, Poland
[4] Department of Chemistry, METU, Ankara, 06800, Turkey
[5] Near East University, Tissue Engineering and Biomaterial Research Center, Nicosia, TRNC, Mersin 10, Turkey
[6] Department of Biological Sciences, METU, Ankara, 06800, Turkey
[7] Department of Medical Engineering, Acibadem University, İstanbul, 34752, Turkey

E-mail: Vasif.Hasirci@acibadem.edu.tr

Keywords: bone tumor model, osteosarcoma, bone tissue engineering, doxorubicin, drug efficacy

Supplementary material for this article is available online

Abstract

We produced a novel three-dimensional (3D) bone tumor model (BTM) to study the interactions between healthy and tumor cells in a tumor microenvironment, the migration tendency of the tumor cells, and the efficacy of an anticancer drug, Doxorubicin, on the cancer cells. The model consisted of two compartments: (a) a healthy bone tissue mimic, made of poly(lactic acid-co-glycolic acid) (PLGA)/beta-tricalcium phosphate (β-TCP) sponge seeded with human fetal osteoblastic cells (hFOB) and human umbilical vein endothelial cells (HUVECs), and (b) a tumor mimic, made of lyophilized collagen sponge seeded with human osteosarcoma cells (Saos-2). The tumor mimic component was placed into a central cavity created in the healthy bone mimic and together they constituted the complete 3D bone tumor model (3D-BTM). The porosities of both sponges were higher than 85% and the diameters of the pores were 199 $\pm$ 52 μm for the PLGA/TCP and 50–150 μm for the collagen scaffolds. The compression Young's modulus of the PLGA/TCP and the collagen sponges were determined to be 4.76 MPa and 140 kPa, respectively. Cell proliferation, morphology, calcium phosphate forming capacity and alkaline phosphatase production were studied separately on both the healthy and tumor mimics. All cells demonstrated cellular extensions and spread well in porous scaffolds indicating good cell–material interactions. Confocal microscopy analysis showed direct contact between the cells present in different parts of the 3D-BTM. Migration of HUVECs from the healthy bone mimic to the tumor compartment was confirmed by the increase in the levels of angiogenic factors vascular endothelial growth factor, basic fibroblast growth factor, and interleukin 8 in the tumor component. Doxorubicin (2.7 μg.ml^{-1}) administered to the 3D-BTM caused a seven-fold decrease in the cell number after 24 h of interaction with the anticancer drug. Caspase-3 enzyme activity assay results demonstrated apoptosis of the osteosarcoma cells. This novel 3D-BTM has a high potential for use in studying the metastatic capabilities of cancer cells, and in determining the effective drug types and combinations for personalized treatments.

1. Introduction

Cancer is a challenging health issue since the clinical success rate is very low. The presence of various types of cancer, their occurrence at different sites in the body, and metastasis to other tissue or organs make the treatment of cancer difficult. Cells of benign cancers do not spread to other tissues, while malignant cancer cells can migrate and metastasize. In the case of bone, although benign tumors do not metastasize they damage the tissue structure and decrease the mechanical strength of the bone [1]. One of the most prevalent

primary malignant bone tumors is osteosarcoma (OS) and this is primarily observed in children and young adults [2]. The survival rate in 5 years is 75% for bone cancers that do not spread from the primary site [3], but for metastatic cases the general survival rate is 40%, and in poor responders to chemotherapy the survival rate is about 20% [3, 4]. The low prevalence of OS and high tumor heterogeneity have hindered the development of novel drugs [5]. An increase in the success of bone cancer treatment is possible through: (i) learning the mechanism of bone cancer pathogenesis; (ii) the development of advanced therapies for bone tumors; and (iii) improvement in drug screening methods to evaluate patient response to available drugs [6]. In order to develop an effective therapy, a model system that closely mimics the tumor environment of the patient would be very valuable, particularly in selecting drugs and dose regimens for a specific patient, in other words, for personalized therapy [7].

We need tissue models which mimic the complex organization of the natural tissue, the extracellular matrix (ECM), and the microenvironment of the cancer cells in the tumor area. The models will help in understanding the underlying mechanisms in cancer occurrence and to develop rational approaches for diagnosis and therapy. In the last five decades, mainly two-dimensional (2D) monolayer tissue cultures have been used to simulate the cancer cell microenvironment and in cancer research [8]. These 2D systems are simple, easy to construct, and convenient for studying cell behavior, however, they poorly mimic the natural tumor microenvironments due to higher oxygen, glucose, and nutrient concentrations, and cause changes in the gene expression, topology, and biochemistry of the cells [9, 10]. In addition, in 2D monolayer cultures the drugs tested show their toxic effects on the cells far more rapidly than in the natural three-dimensional (3D) environment of the cancer tissue [11]. In the 2D environment, due to the absence of interactions with the surrounding stroma, cells growing adherently lose their polarity which also alters several cell responses, such as apoptosis. All these reasons led researchers to derive incorrect conclusions, as is the case in most biologically targeted therapies which perform well in the lab but not in clinics [12].

In the microenvironment of metastatic cancer, the ECM is an important constituent since it has effects on the cancer cell proliferation, migration, and apoptosis by regulating secretion of cytokines and signaling pathways. Furthermore, the ECM associates with cellular components in the native tissue, while a lack of ECM leads to limited cross-talk between metastatic cells and the surrounding tissue [13]. As a result, 3D tissue models which closely mimic the tumor tissue and its microenvironment have become the preferred model types. Some researchers have developed 3D models involving spheroids formed by spontaneous aggregation of the tumor cells on agarose [14], on poly (2-hydroxyethylmethacrylate) (pHEMA) coated plates [15], or on ultralow attachment culture plates [16]. There are some studies on matrix-based 3D tumor models which use hydrogels and sponges to mimic the microenvironment of healthy and tumor tissues. In general, natural-origin materials such as gelatin, collagen, and silk fibroin, or synthetic polymers such as poly(lactic acid) (PLA), poly(glycolic acid) (PGA), poly (ethylene glycol) (PEG), and polycaprolactone (PCL) are used [17–19]. Some studies related to 3D models mimicking bone metastatic cancers (such as breast and prostate cancers) have also been reported. A 3D *in vitro* model was developed by co-culturing prostate cancer cells with osteoblasts on collagen–nanohydroxyapatite scaffolds to study siRNA-based gene delivery systems for the treatment of prostate cancer bone metastasis. It was found that co-culturing reduced the cell proliferation rate in comparison to monoculture and increased the secretion of matrix metallopeptidase 9 enzyme (MMP9), a marker of prostate cancer metastasis [20]. Another construct was prepared by co-culturing human-osteoblast-like cells and human breast adenocarcinoma cells on slowly degradable 3D fibroin scaffolds to study the efficiency of a targeted anticancer drug delivery system on the model [21]. Even though the researchers developed these 3D models to mimic tumors, the healthy bone microenvironment, which has critical importance in tumor initiation and progression, was not taken into account. It is known that the interaction between cancer cells and stromal cells in the bone microenvironment can also lead to resistance to cancer therapy. For example, it was shown that co-culturing of Ewing's sarcoma (ES) cells with Mesenchymal stem cell (MSCs) on PCL scaffolds significantly increased IGF-1 secretion by ES cells through MSC activation of IL-6 and Stat3, which enhanced tumor cell resistance to IGF-1R blockade with the anticancer drug dalotuzumab [22]. There are other 3D bone tumor models (BTMs) based on decellularized or mineralized bone matrices. For example, the importance of the tumor microenvironment was shown in a model of human bone cancer (ES) where tumor cell spheroids were cultured in a bone tissue environment consisting of human mesenchymal stem cells in decellularized bone matrix [23]. In another study, a 3D construct containing both osteoclasts and osteoblasts within a 3D mineralized bone matrix was developed by culturing ES cell spheroids [24]. In many models, the healthy tissue stromal cells are ignored and the absence of interaction between the stromal cells of healthy tissue and the cancer cells of tumor tissue make these models inadequate in mimicking natural bone tumors within healthy bone tissues.

There are some criteria that should be met to show the accuracy of the generated tumor model. For example, pre-vascularization at the initial stages of solid tumor growth, uncontrolled proliferative capacity, formation of regions of hypoxia surrounding a necrotic core, and activation of genetic factors that result in

the recruitment of local endothelial cells for angiogenesis [25]. These points were taken into account when developing our 3D-BTM. The main novelty of our system is the presence of a microenvironment that mimics both the healthy bone and the tumor tissue. In the present study, the model of the bone tumor had osteosarcoma cell seeded collagen sponges (serving as the tumor mimic) inserted in a tissue engineered bone stroma (made of poly(lactic acid-co-glycolic acid) (PLGA)), thus enabling interactions between tumor cells and other tumor cells, the bone tissue matrix, and endothelial cells. In this manner, our biomimetic tumor model involved the primary components required for accurate mimicking *in vivo* conditions in a simple design which would not lead to complex data analysis [26].

The main hypothesis of this study was that a BTM could be constructed with a rigid bone-like exterior carrying healthy cells and a softer, tumor-tissue-like core carrying cancerous cells. In order to reflect the complexity of bone structure, three materials were selected: PLGA and β-tricalcium phosphate (β-TCP) as the organic and inorganic components of the healthy bone, and collagen as the tumorous component. One of our main aims was to study the interaction between healthy and tumor bone cells as in their natural microenvironment. The materials used in the model construction are well established biomaterials, and their properties closely mimic the properties of natural tissue. As the tumor tissue mimic, a cylindrical collagen sponge seeded with human osteosarcoma cells (Saos-2) was prepared. The PLGA/TCP sponge was seeded with both human fetal osteoblastic cells (hFOB) and human umbilical vein endothelial cells (HUVECs). The collagen-based tumor mimic was inserted into a cylindrical cavity at the center of the cylindrical healthy bone mimic to form the complete BTM. The properties and cell–material interactions of each component and the total 3D-BTM were studied. The interaction, communication, and migration of the cells within and between the two compartments of the BTM model were investigated. Then, the model was used to study the efficacy of an anticancer drug, Doxorubicin, in treating cancer in the tumor mimic. One of the major future applications of this model would be to employ it for personalized cancer therapy, in particular, in the determination of effective drug types, combinations, and doses using cancer cells from the specific patient.

2. Materials and methods

2.1. Preparation of the sponges and the 3D-BTM

2.1.1. Preparation of the PLGA/TCP sponges (scaffold of the healthy bone mimic)

Porous PLGA/TCP sponges were prepared by salt leaching and lyophilization. PLGA 82:18 (Corbion, USA) solution (10% w.v^{-1}) was prepared in 1,4-dioxane (Sigma, Germany). β-TCP (Sigma, Germany) was added to it at a concentration of 2.5% w.v^{-1}. Sodium chloride (NaCl) particles (diameter range 150–250 μm) were added into the PLGA/TCP suspension in two different concentrations (PLGA/TCP: NaCl = 1:4 or 1:8 w.w^{-1}). The mixtures were transferred to Teflon molds (figure S1(A), available online at stacks.iop.org/BMM/15/035007/mmedia), frozen at −80 °C, and freeze dried. After leaching the salt in distilled water, the sponges were dried at room temperature (RT). The sponges (external diameter 10 mm and height 6 mm) had a central cavity (diameter 5 mm and depth 4 mm) for the placement of the collagen-based tumor mimic (figure S1(B)).

2.1.2. Preparation of the collagen sponges (scaffold of the tumor mimic)

Collagen type I was isolated from Sprague-Dawley rat tails as described in earlier studies [27, 28]. For the isolation steps, briefly, tendons from rat tails were dissolved in cold acetic acid (0.5 M), filtered, dialyzed against a phosphate buffer, and centrifuged. The collagen pellet was dissolved in acetic acid (0.15 M), precipitated with NaCl solution (5% w.v^{-1}), and then the dialysis and centrifugation steps were repeated. Collagen precipitate was sterilized in ethanol (70%), frozen at −80 °C, and lyophilized. In order to prepare the sponges, collagen solution (1.5% w.v^{-1} in 0.5 M acetic acid) was placed in the Teflon mold (figure S1(C)), frozen at −20 °C and lyophilized. They (figure S1(D)) were then dehydrothermally crosslinked by heating at 140 °C in a vacuum oven [27, 29]. Both sponges were characterized before cell seeding. Then the optimized sponges were seeded with the required cells and brought together to form the BTM.

2.1.3. The 3D-BTM

The PLGA/TCP and collagen sponges were seeded with the required cells and cultured, and then the cell seeded collagen sponge was inserted in its cavity to form the complete BTM (figure S1(E)).

2.2. Characterization of the PLGA/TCP and collagen sponges

2.2.1. Contact angle measurement

The water contact angle of the sponges was measured using a contact angle goniometer (One Attention, Biolin Scientific, Finland). Distilled water (7 μl) was placed at five different locations on the sponges and the contact angles were measured by processing the images using the software of the system.

2.2.2. Degradation

Degradation tests of the PLGA/TCP sponges were conducted by incubation in sterile phosphate buffer saline (PBS) (0.01 M, pH 7.4) containing sodium azide (0.5 mg.ml^{-1}) at 37 °C. Enzymatic degradation of

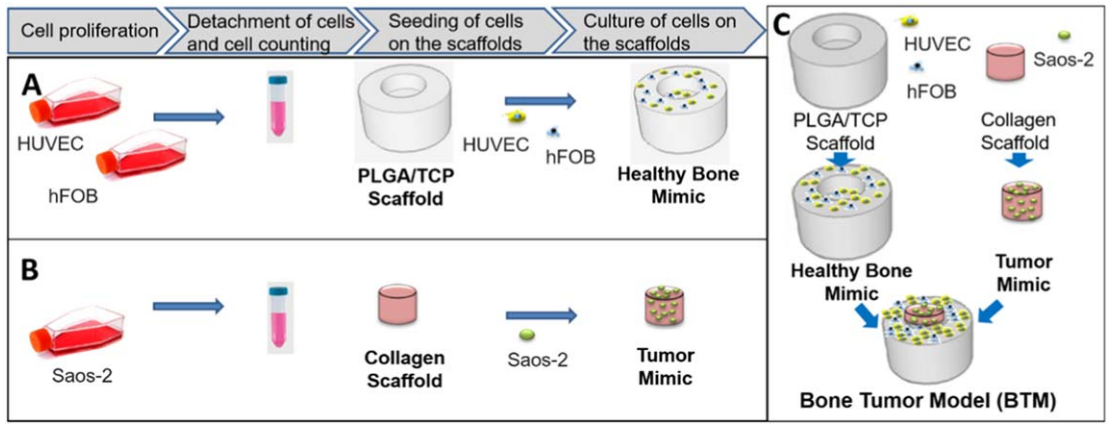

Figure 1. Production of the BTM. Preparation stages of (A) the healthy bone mimic and (B) the tumor mimic. (C) Integration of the tumor mimic in the cavity of the healthy bone mimic to generate the BTM.

uncrosslinked collagen sponges (UXL-CS) and dehydrothermally crosslinked collagen sponges (DHT-CS) were studied in PBS containing collagenase Type II (0.1 mg.ml^{-1}, pH 7.4). The PBS was replaced at every time point. At each time point, the sponges were removed, dried, and weighed. The loss of sample weight was calculated using the equation

$$\text{Weight loss (\%)} = \frac{W_0 - W_1}{W_0} \times 100 \qquad (1)$$

where W_0 and W_1 are the dry weights of the samples at time zero and at various time points, respectively.

2.2.3. Compressive mechanical test

A compression test was performed on the PLGA/TCP and collagen sponges using universal test equipment (Shimadzu AGS-X, Japan, 5 kN load cell) with a compression rate of 0.5 mm.min^{-1}.

2.2.4. Scanning electron microscopy

The samples were placed on carbon tapes (Electron Microscopy Sciences, USA) attached to scanning electron microscopy (SEM) stubs, and coated with Au–Pd. Micrographs were obtained at 10–20 kV using SEM (QUANTA 400F Field Emission SEM, Netherlands) at the METU Central Laboratory.

2.2.5. MicroCT analysis

The samples were scanned using microcomputed tomography (microCT) (Bruker microCT, SkyScan 1172, Belgium). PLGA/TCP sponges were scanned with the application of 100 kV and 100 mA power with an Al 0.5 mm filter and collagen sponges using 35 kV and 21 mA power. Reconstruction was applied using the standard software NRecon. Porosity was determined using CTAn software (CTAn, Bruker microCT). Calcium phosphate deposition on the hFOB/HUVEC seeded PLGA/TCP and cell-free (control) scaffolds were determined using x-ray absorption spectra using the microCT. Control scaffolds without cells were also cultured in the growth medium for 21 days at 34 °C in the CO_2 incubator.

2.3. Cell culture and seeding

HUVECs (C2517A Lonza, USA) were cultured in an EGM-2 BulletKit (Lonza, USA) containing basal medium and a SingleQuots™ Kit at 37 °C in a 5% CO_2 incubator. Human fetal osteoblast cell line, hFOB 1.19 (ATCC, UK), was cultured in DMEM/F12 colorless medium (Gibco, USA) supplemented with fetal bovine serum (FBS) (10%) and G418 (0.3 mg.ml^{-1}) (Sigma, Germany) at 34 °C in a CO_2 incubator. Saos-2 cells (ATCC, UK) were cultured in McCoy's 5 A medium (Lonza, USA) supplemented with FBS (15%) and penicillin/streptomycin (100 Uml^{-1}) (Sigma, USA) at 37 °C in an incubator. Oxygen plasma was applied to the PLGA/TCP (100 W, 3 min) and collagen sponges (100 W, 5 min) to remove the skin layer present on the surface. Samples were sterilized with UV (30 min for each side). HUVECs were detached with Trypsin-EDTA Solution C and hFOB were detached with Trypsin-EDTA Solution B; cells were collected by centrifugation. Equal numbers of each cell type (2×10^5 cells scaffold^{-1}) were seeded on the PLGA/TCP scaffolds, and incubated in a 1:1 ratio of DMEM/F12:EGM-2 at 37 °C in an incubator. Saos-2 cells were seeded on collagen scaffolds (1×10^5 cells scaffold^{-1}) and incubated at 37 °C in a CO_2 incubator. Growth media were refreshed every other day. The steps of cell seeding and the assembly of the tumor mimicking model are presented in figure 1. HUVEC and hFOB cells (1:1) were simultaneously seeded on the outer PLGA/TCP part (healthy bone mimic) (figure 1(A)) while Saos-2 cells were seeded on the inner, collagen, part (tumor mimic) (figure 1(B)). The two scaffolds were cultured separately for 2 days and then were combined (figure 1(C)). For the insertion of the tumor mimic into the healthy bone mimic's cylindrical cavity, the tumor mimic was removed from the culture medium with sterile tweezers and placed into the cavity with extreme care. This bicomponent BTM was

Table 1. qRT-PCR primers and amplicon sizes.

	Primers (5′–3′)	Sequence	Amplicon size (bp)
VEGF	Forward	GAGTACCCTGATGAGATCGAGT	193
	Reverse	ATTTGTTGTGCTGTAGGAAGCT	
bFGF	Forward	ATGGCAGCCGGGAGCATCACC	235
	Reverse	CACACACTCCTTTGATAGACACAA	
IL-8	Forward	CATACTCCAAACCTTTCCAC	165
	Reverse	TCAAAAACTTCTCCACAACC	

cultured in EGM-2:DMEM/F12:McCoy's 5A (1:1:1) medium for 21 days (figure 1(C)). Tissue culture polystyrene (TCPS) plates were used as 2D control surfaces for Alamar Blue and alkaline phosphatase (ALP) assays, and in quantitative PCR analyses.

2.4. Characterization of the healthy bone and tumor mimics

2.4.1. Alamar blue cell viability assay

Cell seeded scaffolds were washed with PBS and incubated with 10% Alamar Blue solution (Invitrogen, USA) in colorless DMEM for 1 h at 37 °C. The absorbances of the 200 μl solutions were measured at 570 nm and 595 nm with a multiwell plate reader (Molecular Devices, USA). The absorbance value was converted to cell number by using percent reduction values and a calibration curve.

2.4.2. ALP activity

A SensoLyte pNPP Alkaline Phosphatase Assay Kit was used to determine the ALP production by hFOB cells on the PLGA/TCP scaffold. Briefly, samples were washed with component B, and lysis buffer was added, frozen, and thawed three times at −80 °C and 37 °C. Sonication (50 W, 20 s) was applied and the contents were centrifuged (2000 rpm, 10 min). The supernatant (50 μl), ALP dilution buffer (50 μl), and Component A (50 μl) were added to each well in 96 well plates, incubated for 1 h at 37 °C and then 50 μl stop solution was transferred to each well. Absorbances were measured at 405 nm by a plate reader. ALP concentration was calculated using the calibration curve.

2.4.3. Immunocytochemistry

The cells present on the scaffolds were fixed by treating them with paraformaldehyde solution (4%) for 15 min at RT. Then they were treated with Triton-X-100 solution (1%) for 5 min and incubated in 1% BSA solution at 37 °C to block nonspecific binding. Samples were stained by incubating in Alexa Fluor 532-Phalloidin for 1 h at 37 °C and DRAQ5 for 15 min at RT. Cell seeded samples were also sectioned with cryomicrotome into 20–30 μm thick slices, and transferred to Polysine™ Microscope Adhesion Slides. Sections were also incubated in Triton-X-100, blocked in the 1% BSA solution, and stained with Alexa Fluor 488 tagged anti-human CD31, Alexa Fluor 532-Phalloidin, and DRAQ5. These samples were examined with a confocal laser scanning microscope (CLSM) (Zeiss LSM 800, Germany).

2.4.4. Scanning electron microscopy

Cell seeded scaffolds were washed twice with PIPES (piperazine-N,N′-bis(ethanesulfonic acid)) buffer, fixed by immersing the samples in paraformaldehyde (4% w.v^{-1}) for 5 min and then lyophilized. Samples were coated with gold–palladium (Au–Pd) under vacuum and examined with SEM (FEI Quanta 200F, USA).

2.5. Construction of the BTM

The hFOB/HUVEC cells were co-cultured on PLGA/TCP scaffolds (as the healthy bone mimic) and Saos-2 cells were cultured on the collagen scaffolds (as the tumor mimic) for 2 days. Then the collagen scaffolds were placed in the central cavity of the PLGA/TCP scaffold and cultured in EGM-2:DMEM/F12:McCoy's 5A (1:1:1) medium for 21 days (figure 1(C)).

2.6. Characterization of the BTM

2.6.1. Immunocytochemistry

Immunostaining was conducted as described in section 2.4.3 on the bicomponent construct. Cryosections were incubated in 1X blocking solution (5% goat serum, 1% Tween 20, 1% BSA and 1% sodium azide in PBS) for 1 h at 37 °C, incubated in anti-CD31 primary Ab (10 μg. ml^{-1} in 0.1X blocking solution) and anti-von Willebrand Factor (vWF) primary Ab (0.05 μg.ml^{-1} in 0.1X blocking solution) at 4 °C overnight, washed with PBS, and incubated in donkey anti-sheep secondary Ab (Alexa Fluor® 594) (0.02 μg.ml^{-1} in 0.1X blocking solution) and goat anti-rabbit secondary Ab (Alexa Fluor® 647) (0.02 μg.ml^{-1} in 0.1X blocking solution) for 1 h at 37 °C. Samples were washed with PBS, incubated in Alexa Fluor 488-Phalloidin for 1 h at 37 °C and in DAPI for 15 min at RT, and examined with a CLSM.

2.6.2. Quantitative real-time PCR analysis of angiogenesis

Angiogenesis was studied using quantitative real-time PCR (qRT-PCR) (Rotor-Gene Q; Qiagen) and a $2^{-\Delta\Delta Ct}$ relative quantification method. Primers were synthesized for vascular endothelial growth factor (VEGF), basic fibroblast growth factor (bFGF), and interleukin 8 (IL-8) genes by Sentegen (Sentegen,

Turkey) according to the sequences presented in table 1. Three types of samples were analyzed: Saos-2 on the control TCPS, Saos-2 on collagen scaffolds alone (coded as Coll), and Saos-2 in collagen scaffolds placed in the cavity of the PLGA/TCP scaffold co-cultured hFOB/HUVEC (coded as Coll/BTM). On days 7, 14, and 21, RNA was isolated using an RNeasy Micro Kit (Qiagen) according to the manufacturer's protocol. The inner collagen sponges of the model were removed from the complete model and cut into small pieces with a scalpel. Then these pieces were incubated in RLT buffer (350 μl) (including 1% β-mercaptoethanol) for 15 min to wet the scaffolds completely. They were vortexed for 15 min in a Falcon tube to disrupt the cells. Then the content of the Falcon tube was added into a QIAshredder spin column for homogenization and were centrifuged (14 000 rpm, 2 min). The isolated RNA samples were treated with DNase I (DNA-free™ Kit; Ambion, Invitrogen, Germany) to prevent DNA contamination and converted to cDNA using a RevertAid First Strand cDNA Synthesis Kit (Invitrogen). qRT-PCR was performed on the cDNA samples obtained.

2.6.3. Agarose gel electrophoresis

The agarose gel (2% in Tris-EDTA buffer solution) was placed in a separator buffer tank, into which the electrodes were placed. Samples were loaded into the wells and a 100 V potential was applied across the electrodes. Samples were run on the gel for 75 min and visualized under UV light (UVP GelDoc Imaging System, USA).

2.7. Efficacy of the anticancer agent tested on the BTM

The BTM was developed as described previously and cultured in EGM-2:DMEM/F12:McCoy's 5A (1:1:1) medium for 7 days. Then, the samples were incubated in medium containing Doxorubicin (2.7 μg.ml^{-1}) for 24 h. The medium was refreshed and incubated for another 24 h. After that, the following efficacy studies were carried out for both the drug-treated samples and the drug-free controls.

2.7.1. Cell number by Alamar Blue assay

Alamar Blue cell viability assay was performed on the samples by modifying a previous Alamar Blue assay procedure. After incubation with the drug for 24 h, the samples were incubated for 3 days in the fresh drug-free medium, 10% Alamar Blue solution in colorless DMEM was added on the samples and then incubated for a further 3 h at 37 °C and under a 5% CO_2 condition. The absorbance of 200 μl solution was measured at 570 nm and 595 nm with a plate reader. Live/dead analyses of the cells were performed using CLSM. For this purpose, the samples were washed with PBS and stained with calcein AM (0.5 μl.ml^{-1} in PBS) for live cells, and ethidium homodimer-1 (2 μl.ml^{-1} in PBS) for dead cells.

2.7.2. Determination of Caspase-3 activity

Caspase-3 activity was determined using a Caspase-3 Activity Kit (Fluorometric) (Abcam, USA) on Doxorubicin-treated BTM according to the manufacturer's protocol. Cell lysis buffer was added on the sample and incubated on ice for 10 min. DTT and DEVD-AFC enzyme substrates were added and the whole solution was incubated for 2 h at 37 °C. Fluorescence intensities at 400 nm (λ_{ex}) and 505 nm (λ_{em}) were measured with a plate reader.

2.8. Statistical analysis

All quantitative data in this study were expressed as mean ± standard deviations with $n \geqslant 3$ unless otherwise stated. Statistical analysis was performed using the GraphPad Prism6 program. Differences between group means were analyzed with Student's *t*-test when the data were normally distributed. Comparisons of groups with one independent variable were performed with one-way ANOVA with Tukey's post-hoc test, to determine significant differences. When there were two independent variables, two-way ANOVA was used. All values are represented as the mean ± standard deviation. Differences of $p < 0.05$ were considered significant.

3. Results and discussion

We prepared a 3D-BTM which mimics a bone tumor together with a healthy microenvironment around the tumor. Each compartment of the BTM was examined separately to optimize the preparation conditions and then combined to form the final 3D tissue model. The healthy and tumor components were prepared from PLGA/β-TCP and collagen. PLGA/β-TCP scaffolds have been used in many studies and demonstrate good cell–material interaction and osteoconductivity [30], enhancement in the bone regeneration of critical bone defects [31], better guidance in the culture of osteoblasts [32], and improvement in biological activity, such as calcium deposition [33]. Thus, β-TCP containing PLGA scaffolds were chosen to represent the healthy component of the model. As the tumor matrix, collagen sponges were selected as collagen constitutes 95% of the organic part of the bone matrix and it is a widely used biomaterial for 3D modeling due to its biocompatibility, biodegradability, and crosslinking capacity [34]. Another reason for choosing two different materials was to mimic the mechanical properties of the model tissues. For trabecular bones, the Young's modulus and compressive strength are 50–100 MPa and 5–10 MPa, respectively [35]. To be able to mimic the structural and mechanical properties of the healthy part of the bone, we used PLGA/TCP which has a compressive modulus value close to that

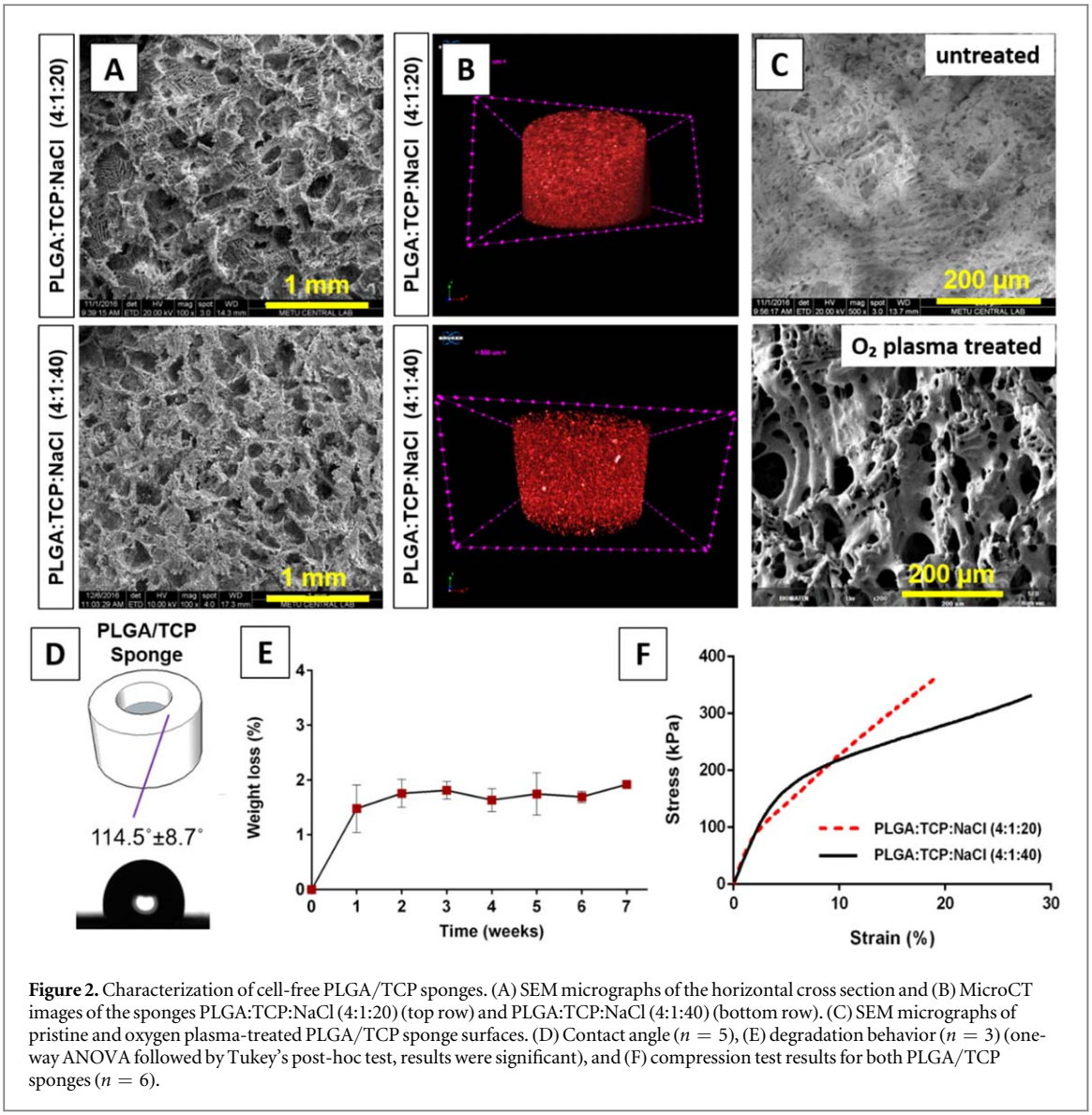

Figure 2. Characterization of cell-free PLGA/TCP sponges. (A) SEM micrographs of the horizontal cross section and (B) MicroCT images of the sponges PLGA:TCP:NaCl (4:1:20) (top row) and PLGA:TCP:NaCl (4:1:40) (bottom row). (C) SEM micrographs of pristine and oxygen plasma-treated PLGA/TCP sponge surfaces. (D) Contact angle ($n = 5$), (E) degradation behavior ($n = 3$) (one-way ANOVA followed by Tukey's post-hoc test, results were significant), and (F) compression test results for both PLGA/TCP sponges ($n = 6$).

of natural bone. On the other hand, the optimal compressive modulus for the osteosarcoma cells was reported as 55 kPa [36]. Collagen which has similar mechanical properties to cancer tissue was used in this study. Detailed characterizations of both scaffolds are given in sections 3.1 and 3.2.

3.1. Properties of the PLGA/TCP scaffolds

The healthy bone mimics were prepared by freeze drying and salt leaching methods using two different NaCl contents with PLGA and TCP together and were coded as PLGA:TCP:NaCl (4:1:20) and PLGA:TCP:NaCl (4:1:40), where the numbers define weight ratios. The average pore size of both scaffolds was about 199 ± 52 μm as determined by the semi-quantitative image analysis ($n \geqslant 20$) mode of ImageJ (NIH, USA), and the porosities determined from the microCT images were 96.7% and 92.6% for the samples PLGA:TCP:NaCl (4:1:40) and PLGA:TCP:NaCl (4:1:20), respectively. The results prove that the presence of higher porogen content (NaCl in our case) was related to higher porosity, in accordance with the literature [37, 38]. These results were also supported by SEM and microCT images (figure 2(A), (B)). SEM also showed that treatment of the samples with O_2 plasma removed the 'skin layer' that generally forms on surfaces during lyophilization and blocks the openings of pores (figure 2(C)) [39, 40]. O_2 plasma-treated PLGA/TCP sponges were used in cell seeding and culture experiments because they had enhanced hydrophilicity and opened pores on the surface as a result of the removal of the skin layer by plasma treatment. The contact angle of the PLGA/TCP scaffold was decreased from $114.5° \pm 8.7°$ to $100.0° \pm 6.1°$ (figure 2(D)). It is reported that anchorage-dependent mammalian cells favor moderately hydrophilic surfaces [41–43]. We have also shown that cells do not prefer to attach to highly hydrophilic or hydrophobic surfaces [44, 45]. Thus the surfaces we obtained were not optimal but they were more suitable for cell seeding than the pristine PLGA/TCP form. Degradation studies showed that the scaffolds were very stable and lost only

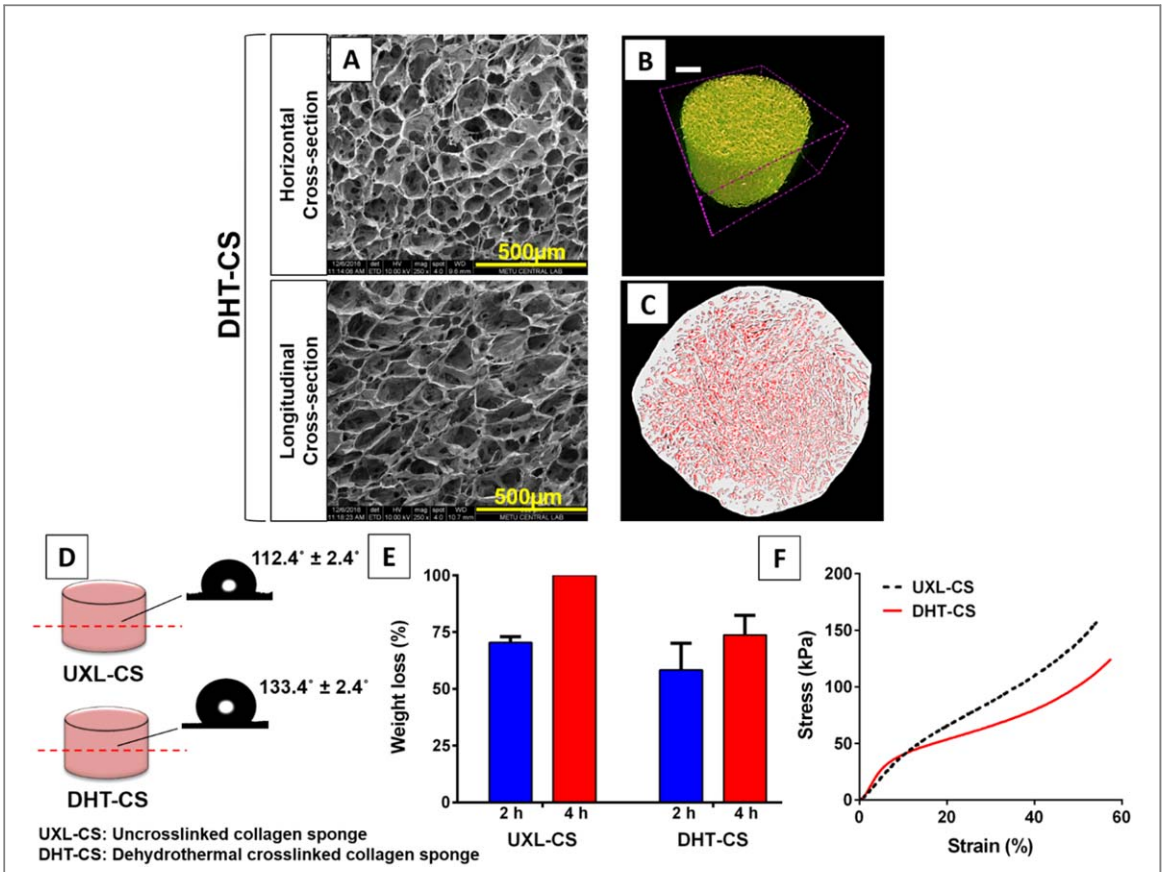

Figure 3. Characterization of the DHT-CS and UXL-CS. (A) SEM micrographs of the horizontal and longitudinal cross sections of the DHT-CS. MicroCT images of the DHT-CS: (B) side view and (C) top view. Scale bar: 250 μm. (D) Contact angles ($n = 5$) (Student's t-test was used, result were significant), (E) enzymatic degradation test ($n = 3$) (Student's t-test was used, result were significant), and (F) compressive mechanical test results of the UXL-CS and DHT-CS ($n = 6$).

about 2% of their weight in 7 weeks incubation in PBS (figure 2(E)). These results also show the suitability of the PLGA scaffolds for long term *in vitro* drug screening tests [46]. The compressive elastic modulus of PLGA:TCP:NaCl (4:1:20) and PLGA:TCP:NaCl (4:1:40) were determined as 5.18 MPa and 4.76 MPa, respectively, showing that the higher porogen (NaCl) content increased the porosity and led to a decrease in the mechanical strength (figure 2(F)). Similar results were also reported by He *et al* for six cylindrical PLLA sponges with different NaCl content. They also showed that higher NaCl particle content led to a higher porosity and lower mechanical strength [37]. It is known that high porosity and pore interconnectivity are essential for cell migration and proliferation, as well as for proper nutrient exchange in the culture medium. The best scaffolds would be those with high and interconnected porosity, and high mechanical strength. Since the difference between the mechanical strengths of the two scaffolds tested was not very high, the sponge with higher porosity, PLGA:TCP:NaCl (4:1:40), was selected for use in further studies.

3.2. Characterization of collagen sponges

Porous collagen sponges prepared by lyophilization were examined using SEM and microCT. The horizontal and longitudinal cross sections of these sponges were very similar without any significant differences (figure 3(A)). All sections had high porosity and interconnectivity as required for efficient transport of nutrients and waste products. The porosities of the sponges were determined from both SEM and microCT data as 96.7% and 86% for PLGA:TCP:NaCl (4:1:40) and collagen sponges, respectively (figures 3(B), (C)). The diameters of the pores were measured using ImageJ (NIH, USA) as 199 ± 52 μm for PLGA:TCP:NaCl (4:1:40) and 50–150 μm for the collagen scaffolds.

In bone tissue engineering, scaffolds are usually produced with pore sizes similar to that of trabecular bone (20–1500 μm) [47]. It was also reported that pores in the range 160–270 μm support rapid and extensive angiogenesis within a scaffold [48]. The pore size of our PLGA:TCP constructs (199 ± 52 μm) which were used to grow hFOB and HUVEC cells is in the range of the ideal pore size for the bone matrix. On the other hand, the osteoblasts were shown to populate more in smaller pores (40 μm) when they were grown in scaffolds with different pore sizes; larger pore sizes (100 μm) facilitated cell migration. Also, the minimum porosity necessary for the regeneration of a blood vessel was reported as 30-40 μm to enable the exchange of metabolic components and to facilitate endothelial cell entrance and 10–100 μm to allow cell infiltration [47]. As a result, the pore size of the

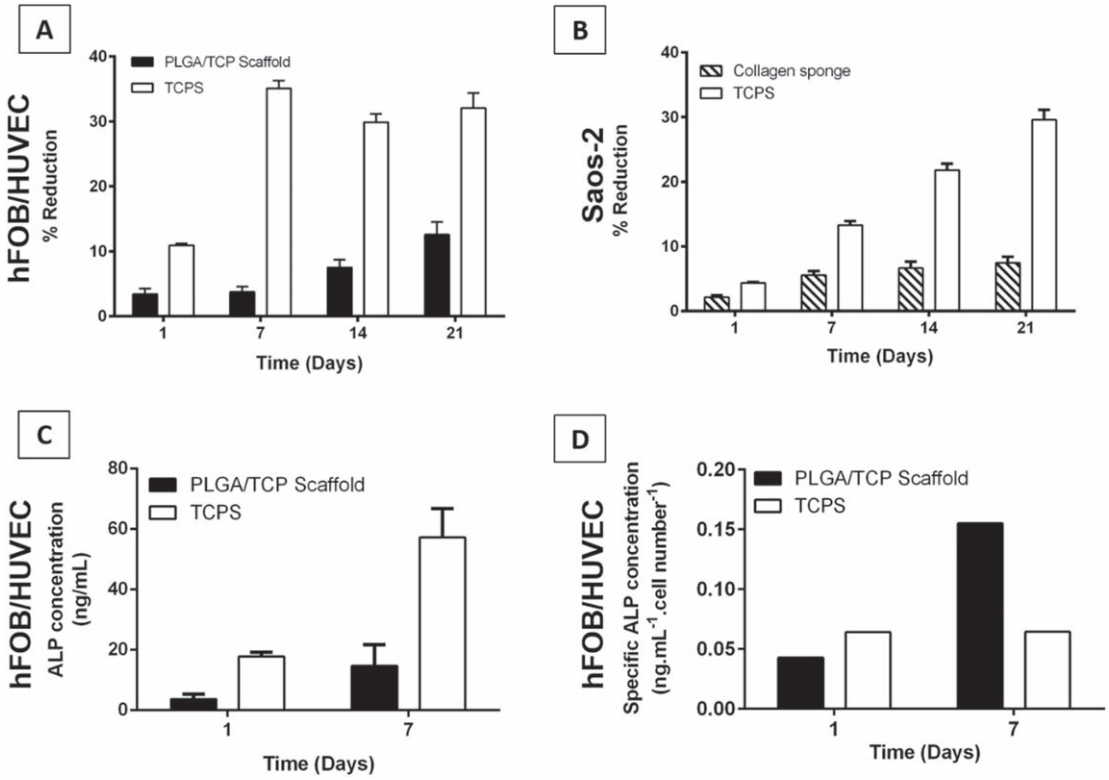

Figure 4. Cell proliferation and ALP activity on the cell seeded PLGA and collagen scaffolds. (A) Proliferation of hFOB/HUVEC on PLGA/TCP scaffolds. (B) Proliferation of Saos-2 on the collagen sponge. (C) ALP activity of hFOB cells on PLGA/TCP scaffolds. (D) Specific ALP activity of the hFOB on PLGA/TCP scaffolds normalized to cell number obtained from Alamar Blue cell viability assay. Seeding densities: hFOB/HUVEC $= 2 \times 10^5$ scaffold^{-1} and Saos-2 $= 1 \times 10^5$ scaffold^{-1}. (A, B, C: two-way ANOVA followed by Sidak' multiple comparison test, $n = 3, p < 0.0001$, the results were significant).

collagen scaffold (50–150 μm) used in our study is suitable for cell growth, infiltration, and migration.

The contact angles of the UXL-CS and DHT-CS were found to be 112.4° ± 2.4° and 133.3° ± 2.2°, respectively (figure 3(D)). These results show that the sponges became more hydrophobic after crosslinking, possibly because during dehydrothermal treatment ester and amide bonds are created either by esterification or amide formation. This decreases the amount of the free carboxyl, amine, and hydroxyl groups, resulting in more hydrophobic materials and leading to the formation of crosslinks between triple helix chains of collagen via condensation reactions [49].

In the enzymatic stability tests, collagenase is used and it breaks the peptide bonds of collagen and causes destruction of the ECM [50]. After 2 h incubation in collagenase solution, the weight loss for the UXL-CS (70.5% ± 2.5) was higher than for the DHT-CS (58.3% ± 11.8). When we extended the treatment from 2 h to 4 h, the UXL-CS completely disintegrated while the DHT-CS lost a large fraction (73.8% ± 8.6) of its initial weight (figure 3(E)). A higher degree of stability (and therefore degradation) of the DHT-CS was expected due to the crosslinking treatment.

The compressive elastic moduli of the UXL-CS and DHT-CS were 111 ± 18 kPa and 140 ± 46 kPa as measured from the initial slopes of stress–strain curves. This shows that crosslinking enhanced the mechanical strength of the sponges in addition to increasing their stability (figure 3(F)).

Based on these results, the DHT-CS was selected as the matrix to culture Saos-2 cells and to serve as the tumor mimic.

3.3. Properties of the tumor and healthy bone mimics

3.3.1. Cell proliferation and ALP activity

Alamar Blue assay was performed on the hFOB/HUVEC cells (1:1) seeded on the PLGA/TCP scaffold to study cell proliferation (figure 4(A)). The cell seeding density was 2×10^5 cells and on Day 1 approximately 2.7×10^5 cells were counted on the TCPS control while fewer (8.7×10^4) cells were determined on the PLGA/TCP scaffold. The cell number on the scaffold increased gradually over time, while on the TCPS the cell number rapidly reached a plateau in a week, indicating confluence.

Alamar Blue assay was also performed for Saos-2 cells seeded on the collagen scaffold (figure 4(B)). The cell seeding density was half that of the hFOB/HUVEC (1×10^5). The rate of proliferation of Saos-2 on the TCPS was higher than on the collagen. The cell numbers increased on both collagen and TCPS for 3 weeks.

The ALP activity of hFOB on the PLGA/TCP scaffold was determined on Days 1 and 7 (figure 4(C)). It increased during the 7 day incubation; however, ALP activity on the scaffold was about three times lower than on the control. Since the cell numbers were not the same on different scaffolds, the ALP values were normalized by dividing the results with the cell numbers. The normalized ALP activity on Day 7 was significantly (about two-fold) higher (figure 4(D)), showing that the cells on the sponges could produce significant amounts of ALP.

3.3.2. Microscopy and microCT results

The nuclei and cytoskeletons of the cells were stained to study the cell morphology, intercellular interaction, and cell–material interactions using CLSM and SEM. From Day 7 onwards, the cells spread over the surface and covered it completely (figure 5(A)). They showed filamentous extensions (filopodia) indicating interaction with the surface (figure 5(B)). Anti-human CD31 immunostaining of HUVECs on the PLGA/TCP scaffolds (figure 5(C)) showed expression of CD31. Since this protein is excreted in high levels by early and mature endothelial cells, it is used to show the presence of HUVECs on the specimen [51]. The CD31 staining in our samples proves the presence of the HUVECs which were seeded on the scaffolds. The staining of actin and nuclei also shows that both HUVECs and hFOB exist on the section, which were also seeded on the scaffolds. Calcium phosphate (CaP) crystals produced by cells in addition to the TCP particles introduced during scaffold production are observed as white spots on the microCT images (figure 5(D)). However, it is not possible to distinguish those produced by the cells and those introduced during scaffold production from each other.

Changes in porosity were observed upon cell seeding and over the culture duration. The 96.7% porosity of unseeded PLGA/TCP scaffolds decreased with time to 89.6%, 90.2%, and 85.7% on Days 7, 14, and 21, respectively. This decrease in porosity is probably because of the filling of the pores by the production of the new ECM and deposition of new calcium phosphate by the cells [52]. The peaks on the x-ray absorption spectra of hFOB/HUVEC seeded PLGA/TCP scaffolds were also higher than for the cell-free scaffolds (figure 5(D), right) and are most probably due to calcium phosphate deposition by cells. The CLSM results for Saos-2 cells on the collagen tumor mimic are shown in figures 5(E)–(H). The cells started to spread, fill the pores of the collagen sponge, and interact with each other as the incubation time increased (figure 5(E)). On Days 14 and 21, the coverage is more extensive and the cells appear to be organized in the form of a layer. These increases were also indicated by the Alamar Blue assay of the Saos-2 cells (figure 4(B)). Here, the cell number did not increase further, possibly because of the confluence of the cells. Cells interacted with the surface with their filopodia (figure 5(F)). It is also seen that the cells had migrated and attached to the walls of the pores at the core of the sponge (figure 5(G)). MicroCT analysis shows the calcium phosphate forming capacities of the cells (figure 5(H)).

The presence of cells, their proliferation and secretion of calcium phosphate affected the porosity of the collagen sponges as they did in the PLGA scaffolds. The porosity of cell-free collagen sponge was 86%, which decreased to 73% and 56% after 7 days and 3 weeks of culturing, respectively. When microCT images of horizontal cross sections of the unseeded and cell seeded sponges were investigated, the exterior of the collagen sponge where cells proliferated and formed cell clusters appeared brighter than the core of the sponges (figure 5(H)). The x-ray absorption of the unseeded sample (examined along the red line) is almost linear, demonstrating the homogeneous composition of the collagen sponge (figure 5(H), right).

3.4. Properties of the complete 3D-BTM

3.4.1. Microscopy results

The complete 3D-BTM has two compartments and is formed by combination of a tumor mimic and a healthy bone mimic. The experiments carried out seperately on individual sponges (PLGA and collagen) were also performed on the BTM. The cell nuclei and cytoskeleton were stained and since the dyes stained the cells indiscriminately, the different cell types could not be distinguished from each other (figures 6(A)–(D)). Cells on the BTM attached, spread, and covered the surfaces of the scaffolds by Day 21. In figures 6(E)–(H), samples were stained with anti-vWF (red) and CD31 antibody (pink) dyes, both of which are specific for HUVECs. The cytoskeleton (green) and nucleus (blue) of the cells were also stained. Due to the specificity of these dyes, it became possible to distinguish HUVECs from the other two cell types, and they were detected on the exterior and the top surface of the collagen sponge (figures 6(E), (F)) in addition to the exterior and bottom surfaces of the PLGA/TCP scaffold (figures 6(G), (H)). Since HUVECs and hFOB were seeded only on the PLGA/TCP scaffolds, the presence of HUVECs on the PLGA/TCP scaffold was expected, but their detection on the collagen sponge demonstrates that these cells have migrated from the healthy bone mimic to the tumor mimic area. This migration of the HUVECs to the cancer component was an indication of the angiogenic process which precludes the vascularization of the tumor tissue as happens in native biological systems [53]. Spreading and coverage of the surfaces of the sponges by hFOB, HUVECs, and Saos-2 was also shown by the SEM micrographs (figures 6(I)–(L)). Horizontal sections of the BTM (figures 6(M), (N)) were stained to show the migration of HUVECs to the core of the cancer mimic

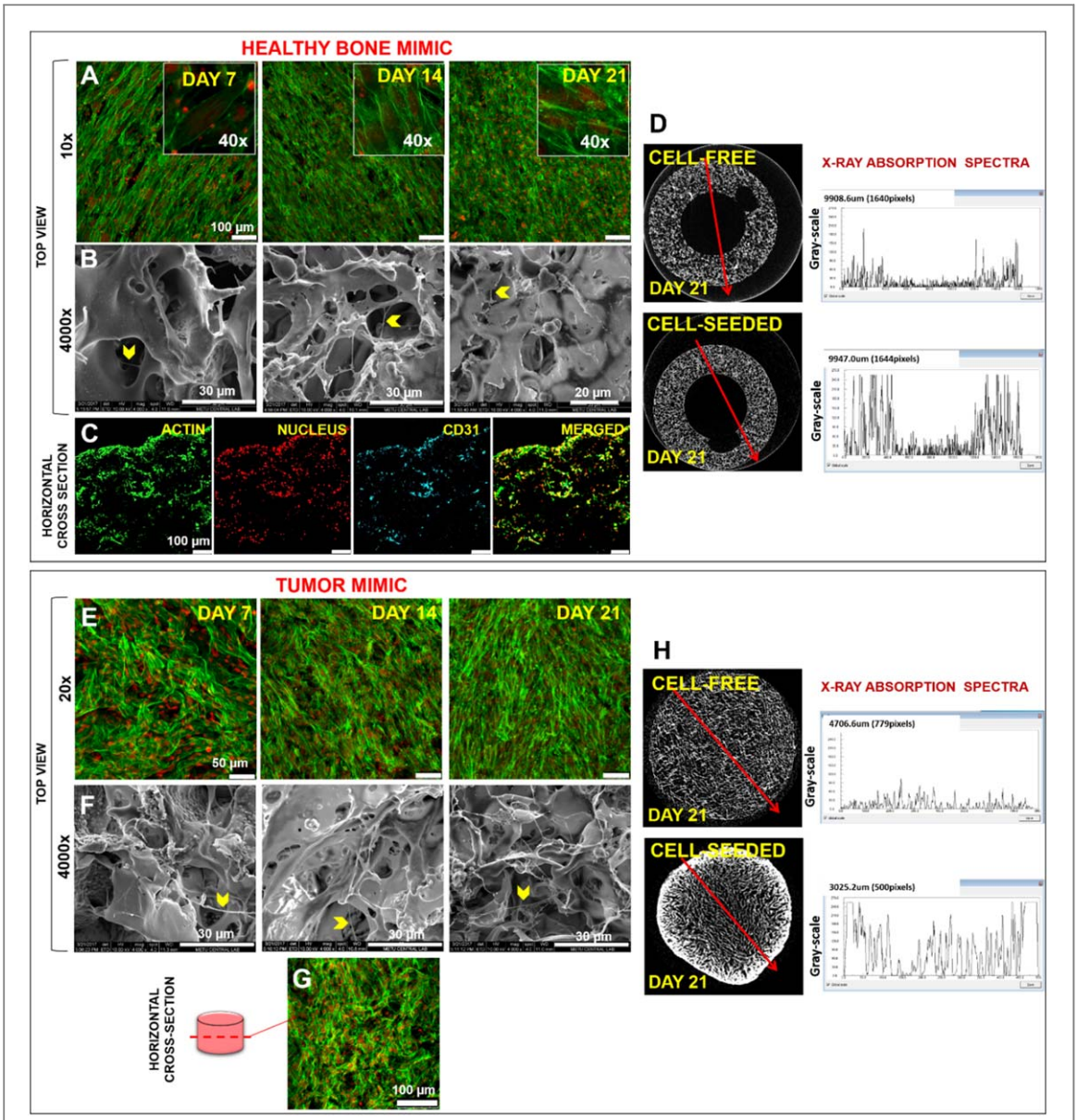

Figure 5. CLSM, SEM, and microCT analysis results. (A) CLSM and (B) SEM micrographs of hFOB and HUVECs on the PLGA/TCP scaffold on Days 7, 14, and 21. (C) CLSM micrographs of the horizontal cross section of PLGA/TCP scaffolds on Day 28. (D) MicroCT images (top view) and x-ray absorption spectra of the horizontal cross section of the healthy bone mimic. (E) CLSM and (F) SEM micrographs of the Saos-2 on collagen scaffolds on Days 7, 14, and 21. (G) CLSM micrograph of a horizontal cross section of the collagen scaffold. (H) MicroCT images (top view) and x-ray absorption spectra of horizontal cross sectional views of the tumor mimic. Cell seeding densities $= 1 \times 10^5$ Saos-2 scaffold^{-1} and 2×10^5 hFOB + HUVEC scaffold^{-1}. The stains were Alexa Fluor 532-Phalloidin (green): actin; DRAQ5 (red): nucleus; and Alexa Fluor 488 anti-human CD31 (blue): CD31. Yellow arrowheads indicate filamentous cell extensions (filopodia). The red lines show the direction in which the spectra were taken.

(collagen). Cells of the healthy bone mimic were mainly detected in the regions that are in direct contact with the collagen core, the cancer mimic. HUVECs (pink) that have migrated into the tumor area are clearly seen in figure 6(N) (a magnified image of figure 6(M)). The direct contact between the scaffolds apparently allowed the migration of the endothelial cells to the tumor side as if to vascularize the tumor. This is a good indicator that the model works. The microCT of the horizontal section of the BTM also showed this direct contact between the two regions, indicating that this model has a good potential to mimic cancer tissue (figure 6(O)).

3.4.2. Molecular analysis of angiogenesis

The expression of angiogenic factors (VEGF, bFGF, and IL-8) in the BTM was studied with qRT-PCR for 21 days (figure 7). In this analysis, three types of samples were used: Saos-2 cells cultured on (1) TCPS (control group), (2) collagen sponge, and (3) collagen sponge in the BTM.

At certain time points, the collagen sponges were treated for RNA isolation and qRT-PCR analysis. In the case of the BTM model, the collagen sponge was removed and the relative expression levels of angiogenic factors of the BTM (Group 3) and that of the collagen sponge alone (Group 2) were determined. Any

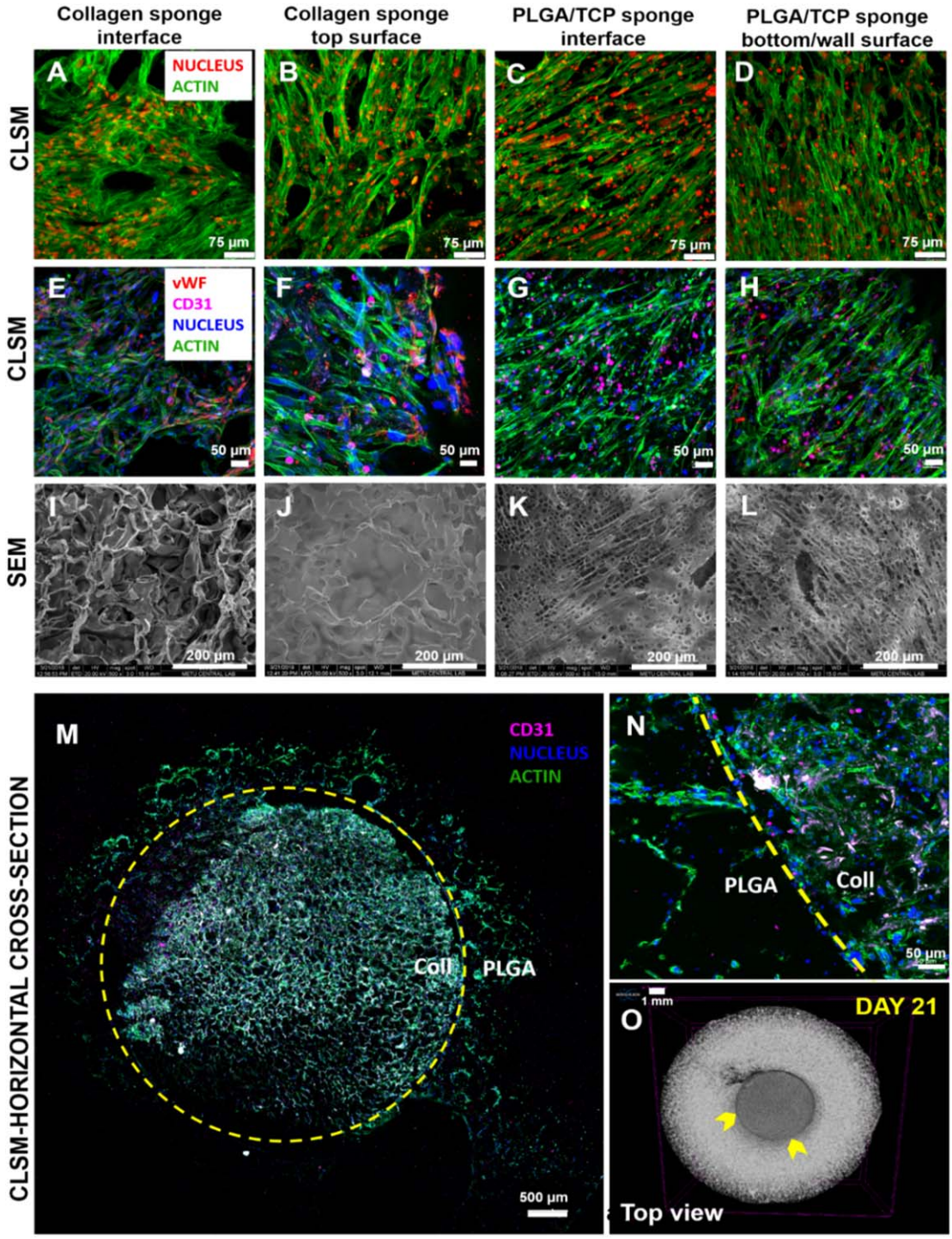

Figure 6. CLSM and SEM analysis of the BTM. (A)–(D) CLSM micrographs of actin and nucleus staining, and (E)–(H) antibody staining. (I)–(L) SEM micrographs of hFOB, HUVECs, and Saos-2 on PLGA/TCP and collagen scaffolds on Day 21. Alexa Fluor 532-Phalloidin (green) stains actin and DRAQ5 (red) stains the nucleus of all types of cells in figures (A)–(D). Alexa Fluor 488-Phalloidin (green) stains actin, DAPI (blue) stains the nucleus of all types of cells, and anti-CD31 antibody (pink) and anti-vWF antibody (red) stain HUVECs in figures (E)–(H). (M), (N) CLSM micrographs and (O) microCT image of a horizontal section of the BTM. Yellow arrowheads and yellow dashed lines show the interface between the two mimics. Alexa Fluor 488-Phalloidin (green) stains actin and DAPI (blue) stains the nucleus of all types of cells. Anti-CD31 antibody (pink) stains HUVECs.

changes in the expression of angiogenic factors were accepted as the combined contribution of HUVEC cells migrated into the tumor mimic of the BTM and the Saos-2 cells already present there. Thus, the presence of angiogenic factors in the tumor region indicates the initiation of vascularization in the model. The relative VEGF and bFGF gene expression levels are presented in figures 7(A), (B). The gene expression level of Saos-2 cells cultured on TCPS served as a reference. No significant differences were detected in the VEGF expression on Days 7, 14, and 21 for Saos-2 cells cultured in collagen sponges. On the other hand, in the BTM, VEGF expression by Saos-2 was significantly high on Day 7. The literature states that the presence of

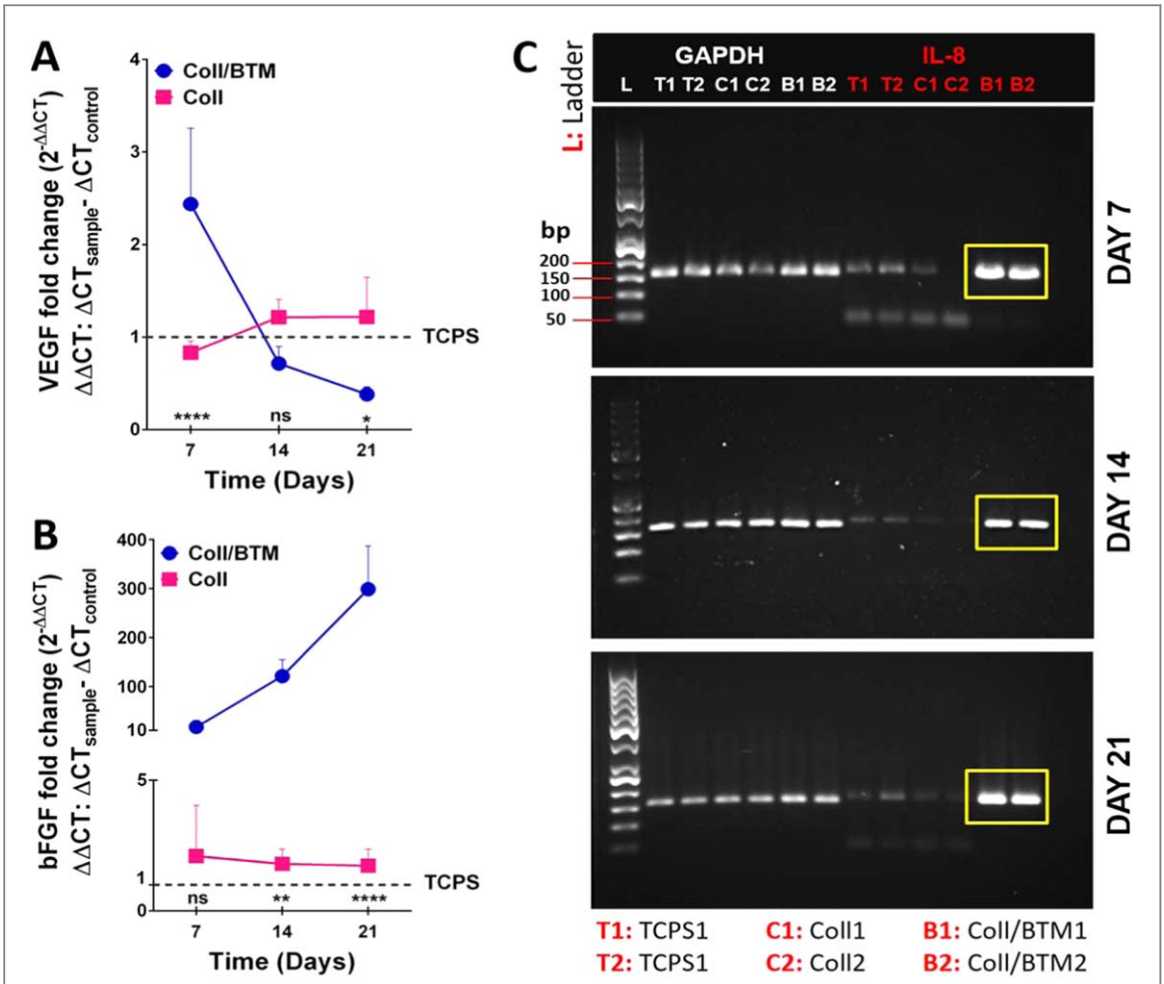

Figure 7. Analysis of the angiogenesis of the BTM. Relative expression levels of (A) VEGF and (B) bFGF genes, and (C) agarose gel electrophoresis of IL-8 genes of Saos-2 cells on the TCPS surface (TCPS), collagen sponge (Coll), and collagen sponge in the BTM (Coll/BTM) on Days 7, 14, and 21. Yellow rectangles show the cDNA bands corresponding to IL-8 mRNA of Saos-2 in Coll/BTM. Statistical analysis between samples (Coll and Coll/BTM) was carried out using two-way ANOVA. $^{*}p < 0.05$, $^{**}p < 0.01$, $^{****}p < 0.0001$, ns = not significant, $n = 6$.

the healthy bone mimic around the tumor tissue affects the expression level of VEGF and tumor progression, as was observed in our study [54, 55]. VEGF is a powerful angiogenic factor, and it is generally believed that tumor cells secrete VEGF to enhance the formation of their own vascular network [56]. It stimulates the formation of new blood vessels and controls apoptosis and differentiation of tumor cells and osteoblasts. It has an effect on tumor progression and pathological remodeling. However, the VEGF expression level in the later days decreased, probably as a result of a negative feedback mechanism. As reported in some studies [57–59], there are some negative regulators that influence angiogenesis in an autocrine manner, leading to downregulation of VEGF. Some of these regulators are directly induced by stimulators of angiogenesis, in particular VEGF, as a consequence of a specific negative-feedback regulator mechanism of angiogenesis [60]. There was also no significant difference in bFGF expression by Saos-2 cells in the collagen sponge alone, but in the case of the BTM these values were higher by approximately 10, 110, and 300 times on Days 7, 14, and 21, respectively. These high levels and the substantial increase are probably a synergic effect of the interactions and cross-talk between the hFOB and HUVECs seeded into the model.

IL-8 has some critical effects on pro-angiogenic, pro-migratory, and osteoclastogenic activities. Many cancerous cell types express IL-8, resulting in proliferation and migration of cancer cells and tumor angiogenesis and metastasis, and researchers have shown that highly metastatic solid tumors express IL-8 [61]. In this study, the relative IL-8 gene expressions of the samples could not be calculated because the expression levels of Saos-2 on the TCPS surface and collagen sponge were too low for quantification with qRT-PCR. For this reason, the IL-8 gene expression in BTM was demonstrated by agarose gel electrophoresis. Micrographs show significantly high levels of IL-8 expression in the BTM on Days 7, 14, and 21 (figure 7(C)). Tan *et al* co-cultured U2OS osteosarcoma cells with immortalized fibroblasts or HUVECs to study the effect of 3D structure (silk scaffolds) and tumor–stroma interaction, and reported that the co-culture of U2OS osteosarcoma cells with immortalized fibroblasts resulted in the upregulation of angiogenic factors (VEGF, IL-8, bFGF) and particularly that of

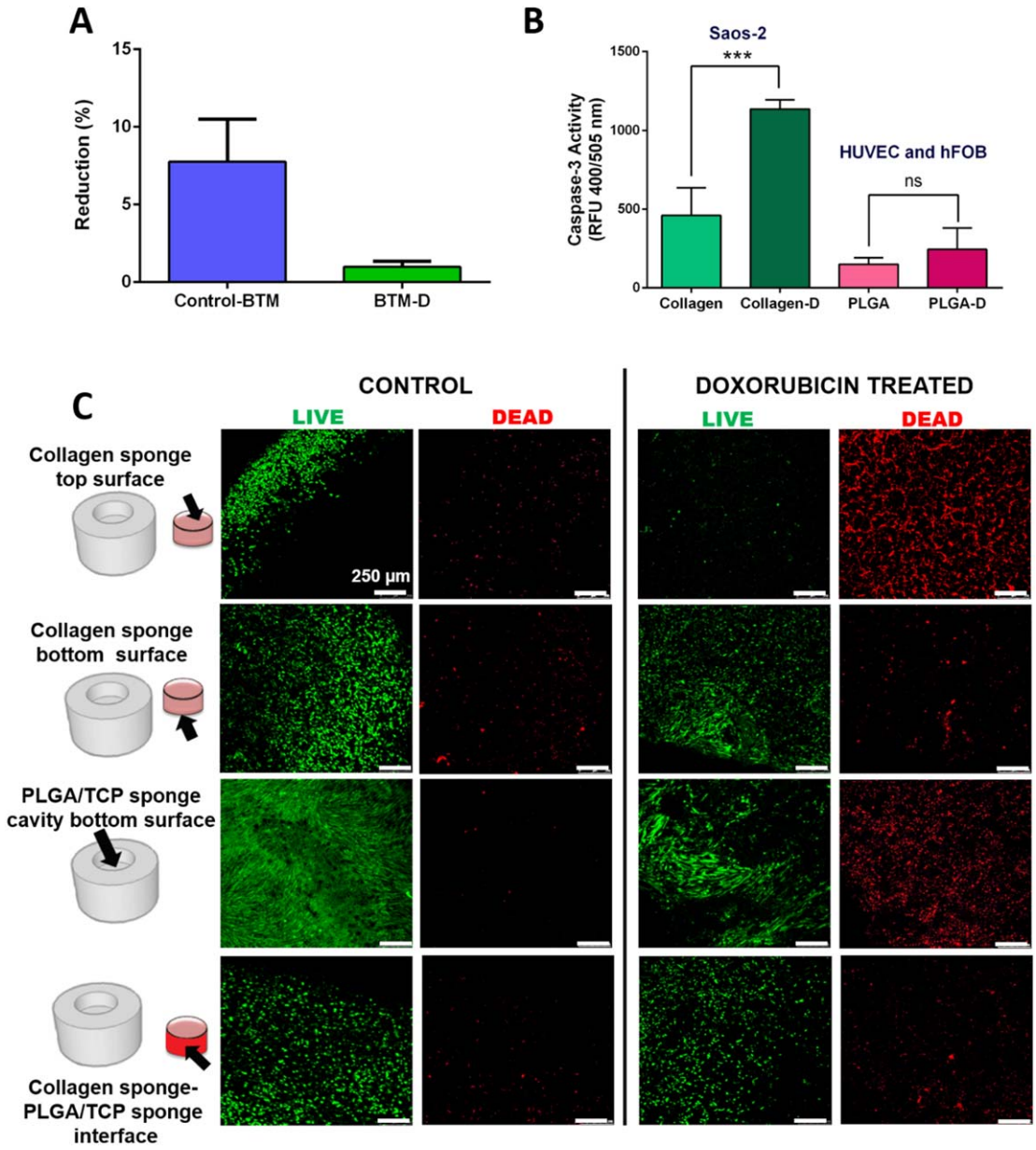

Figure 8. Efficacy of Doxorubicin on the BTM. (A) An Alamar Blue cell viability assay of the Doxorubicin-treated (BTM-D) and untreated BTM (Control-BTM). The reduction (%) of the dye is proportional to the live cell number. (B) Caspase-3 enzyme activity. (C) Cell viability assay of the Doxorubicin-treated and untreated BTM using live/dead staining. CLSM micrographs of stained cells on different parts of the model are given. Calcein AM (green) shows viable cells and ethidium homodimer-1 (red) shows nonviable cells. Scale bar $= 250$ μm for all images. (A: Student's t-test, $n = 3$, results were significant; B: one-way ANOVA followed by Tukey's post-hoc test, results were significant $^{***}p < 0.001$; and ns: not significant, $n = 3$).

IL-8 [62]. In the present study, co-culture of Saos-2, in close vicinity of hFOB and HUVECs, significantly upregulated the IL-8 expression. As a result, we showed that the expression of pro-angiogenic factors increased significantly in the two-compartment novel BTM, indicating the success of mimicking the natural tissue.

3.5. Study of the efficacy of an anticancer agent on cell viability in the BTM

In order to assess the suitability of the constructed BTM to serve as a cancer tissue model, Doxorubicin (a drug used in osteosarcoma therapy) was added into the system and its effectiveness on the viability of the cells was studied. Initially, a dose–response curve was prepared *in vitro* with Saos-2 cells in a tissue culture plate exposed to a range of concentrations of the drug. The dose–response curve (figure S2) showed that the IC_{50} value of Doxorubicin was 0.1876 $\mu g.ml^{-1}$ when the seeding density was 2×10^4 cells per well. Since the number of cells on the BTM (3×10^5 cells) was almost 15-fold higher than on the TCPS wells (2×10^4 cells), a 15-fold higher drug concentration (2.74 $\mu g.ml^{-1}$ Doxorubicin) was used on the model. An Alamar Blue cell viability test showed that the cell number was significantly decreased following treatment with Doxorubicin (figure 8(A)). Caspase-3 enzyme activity is an indicator of apoptosis

and figure 8(B) shows the activity (thus the amount) of the caspase-3 enzyme in the Doxorubicin-administered BTM. Doxorubicin was applied to the bicomponent BTM, and then the two cell seeded sponges (exterior PLGA and core collagen) were separated from each other for the analysis of the enzymatic activity on each component. A significant increase in caspase-3 activity was determined in the collagen sponge, while there was no significant change in the healthy bone tissue mimic. It was expected that the drug would be more effective on the cancer tissue mimic because of the cancer cells loaded in it. A live/dead assay also showed lower viability in the Doxorubicin-treated model than in the untreated model (figure 8(C)). Doxorubicin was more effective at the top surface of the collagen sponge, possibly because this part of the model was in more direct contact with the drug-containing culture medium (figure 8(C), top row). A drug dose killing all the cells in the tissue culture plates but only a portion in the BTM is also a good indicator of the difference in the effect of drugs on 2D and 3D cultures. Apparently, the cells in the culture plate (the 2D environment) are more exposed to the culture conditions while in the 3D-BTM model the microenvironment prevents such direct effects. In figure 8(C), the collagen sponge bottom surface and the PLGA/TCP sponge cavity bottom surface are not in direct contact with the drug-containing medium and so the number of affected cells is lower than those at the top surface of the collagen sponge. It can, therefore, be concluded that the BTM developed in this study mimics a bone tumor. Of course, further experiments are needed to optimize the parameters before initiating any patient specific human trials.

The results presented in this study show that the BTM could mimic a natural osteosarcoma and could be considered for use in studying the efficacy of different types of drugs on cells obtained from a patient for 'patient specific treatment'. However, before use in clinical applications, several optimization steps should be taken. In this model, proliferation of Saos-2 cells and their interactions with HUVECs were studied. In the literature, there are studies carried out with spheroids and it is known that cells in spheroids have strong cell–cell interactions and a different morphology than cells in a 2D monolayer culture. Interactions between cells in 3D spheroids were also reported to increase their stability and survival rates, indicating resistance to anticancer agents [11, 14, 63]. Thus, new studies with spheroids need to be performed by loading them in the core collagen instead of loading individual cells. Studies along these lines are in progress.

Another limitation of the current model is the use of cell lines instead of a patient's own cells. Even though the use of cell lines under *in vitro* conditions provides valuable insights on tumor development and on the mechanisms of therapeutic applications, the main drawback of using cancer cell lines is their lack of both phenotypic and genetic heterogeneity, which is observed when cancer cells are obtained from the patient. Thus, in the future, this model could be used to yield more realistic results if seeded with cells derived from bone cancer patients.

4. Conclusion

In this study, a functional 3D bone tumor model (BTM) was successfully developed by combining two components: (1) a tumor mimic consisting of osteosarcoma (Saos-2) cells seeded in a collagen sponge and (2) a healthy bone mimic that was formed by seeding hFOB and HUVECs in PLGA/TCP sponge. This model aimed to mimic the *in vivo* tumor stroma by providing not only the cross-talk between the cancer cells, but also the interactions of cancer cells with the healthy bone cells and the bone matrix. The natural bone tumor microenvironment constructed in this manner led to cancer cells increasing their expression of angiogenic factors when cultured in the BTM model. Direct contact between the healthy bone cells (hFOB and HUVECs) and cancer cells (Saos-2) was achieved, and when treated with the anticancer agent, Doxorubicin, the effect was observed specifically on the cancer cells. These indicate that this new strategy in tumor modeling, with tumor cells cultured within an engineered bone construct, could create a microenvironment similar to that of the native tissue. In conclusion, we believe the 3D-BTM developed in this study could be a good candidate for screening tests for drug efficacy. This will also be a promising approach in personalized drug therapy for finding the right type, combination, and dose regimen of drugs for a specific individual.

Acknowledgments

The authors would like to thank TUBITAK for support through Project No: 215M621 and Grant BIDEB2211-C, and A K acknowledges scholarships through the same. The authors are also grateful to BIOMATEN, METU Center of Excellence in Biomaterials and Tissue Engineering for support and use of their facilities.

Disclosure

The authors declare no conflict of interest.

ORCID iDs

Ezgi Antmen https://orcid.org/0000-0003-1271-4644
Nesrin Hasirci https://orcid.org/0000-0002-4497-0194
Vasif Hasirci https://orcid.org/0000-0002-3698-8861

References

[1] Misaghi A, Goldin A, Awad M and Kulidjian A A 2018 Osteosarcoma: a comprehensive review *SICOT-J* **4** 12

[2] Rogers K M and Conran R M 2019 Educational case: pediatric osteosarcoma *Acad Pathol.* **6** 1–5

[3] Verrecchia F and Rédini F 2018 Transforming growth factor-β signaling plays a pivotal role in the interplay between osteosarcoma cells and their microenvironment *Front. Oncol.* **8** 133

[4] Botter S M, Neri D and Fuchs B 2014 Recent advances in osteosarcoma *Curr. Opin. Pharmacol.* **16** 15–23

[5] Zhu L, McManus M M and Hughes D P 2013 Understanding the biology of bone sarcoma from early initiating events through late events in metastasis and disease progression *Front. Oncol.* **3** 230

[6] Díaz E C G, Sinha S, Avedian R S and Yang F 2019 Tissue-engineered 3D models for elucidating primary and metastatic bone cancer progression *Acta Biomater.* **99** 18-32

[7] Kondo J and Inoue M 2019 Application of cancer organoid model for drug screening and personalized therapy *Cells* **8** 470

[8] Duval K, Grover H, Han L-H, Mou Y, Pegoraro A F, Fredberg J and Chen Z 2017 Modeling physiological events in 2D vs 3D cell culture *Physiology* **32** 266–77

[9] Pampaloni F, Reynaud E G and Stelzer E H K 2007 The third dimension bridges the gap between cell culture and live tissue *Nat. Rev. Mol. Cell Biol.* **8** 839–45

[10] Chhetri A, Chittiboyina S, Atrian F, Bai Y, Delisi D A, Rahimi R, Efremov Y, Park K, Talhouk R and Lelièvre S A 2019 Cell culture and coculture for oncological research in appropriate microenvironments *Curr Protoc Chem Biol.* **11** e65

[11] Lama R, Zhang L, Naim J M, Williams J, Zhou A and Su B 2013 Development, validation and pilot screening of an *in vitro* multi-cellular three-dimensional cancer spheroid assay for anti-cancer drug testing *Med. Chem.* **21** 922–31

[12] Lamhamedi-Cherradi S E, Santoro M, Ramammoorthy V, Menegaz B A, Bartholomeusz G, Iles L R, Amin H M, Livingston J A, Mikos A G and Ludwig J A 2014 3D tissue-engineered model of Ewing's sarcoma *Adv. Drug Deliv. Rev.* **79–80** 155–71

[13] Verjans E T, Doijen J, Luyten W, Landuyt B and Schoofs L 2018 Three-dimensional cell culture models for anticancer drug screening: worth the effort? *J. Cell. Physiol.* **233** 2993–3003

[14] Charoen K M, Fallica B, Colson Y L, Zaman M H and Grinstaff M W 2014 Embedded multicellular spheroids as a biomimetic 3D cancer model for evaluating drug and drug–device combinations *Biomaterials* **35** 2264–71

[15] Martins-Neves S R, Lopes Á O, do Carmo A, Paiva A A, Simões P C, Abrunhosa A J and Gomes C M 2012 Therapeutic implications of an enriched cancer stem-like cell population in a human osteosarcoma cell line *BMC Cancer.* **12** 139

[16] Baek N, Seo O W, Kim M, Hulme J and An S S A 2016 Monitoring the effects of Doxorubicin on 3D-spheroid tumor cells in real-time *Onco. Targets. Ther.* **9** 7207–18

[17] Fong E L S *et al* Modeling Ewing sarcoma tumors *in vitro* with 3D scaffolds *Proc. Natl Acad. Sci. USA* 2013 **110** 6500–5

[18] Tan P H S, Aung K Z, Toh S L, Goh J C H and Nathan S S 2011 Three-dimensional porous silk tumor constructs in the approximation of *in vivo* osteosarcoma physiology *Biomaterials* **32** 6131–7

[19] Fallica B, Maffei J S, Villa S, Makin G and Zaman M 2012 Alteration of cellular behavior and response to PI3K pathway inhibition by culture in 3D collagen gels *PLoS One* **7** e48024

[20] Fitzgerald K A, Guo J, Raftery R M, Castaño I M, Curtin C M, Gooding M, Darcy R, O'Brien F J and O'Driscoll C M 2016 Nanoparticle-mediated siRNA delivery assessed in a 3D co-culture model simulating prostate cancer bone metastasis *Int. J. Pharm.* **511** 1058–69

[21] Subia B, Dey T, Sharma S and Kundu S C 2015 Target specific delivery of anticancer drug in silk fibroin based 3D distribution model of bone–breast cancer cells *ACS Appl. Mater. Interfaces* **7** 2269–79

[22] Santoro M, Menegaz B A, Lamhamedi-Cherradi S E, Molina E R, Wu D, Priebe W, Ludwig J A and Mikos A G 2017 Modeling stroma-induced drug resistance in a tissue-engineered tumor model of Ewing sarcoma *Tissue Eng. Part* A **23** 80–9

[23] Villasante A, Marturano-Kruik A and Vunjak-Novakovic G 2014 Bioengineered human tumor within a bone niche *Biomaterials* **35** 5785–94

[24] Villasante A, Marturano-Kruik A, Robinson S T, Liu Z, Guo X E and Vunjak-Novakovic G 2017 Tissue-engineered model of human osteolytic bone tumor *Tissue Engineering* C **23** 98–107

[25] Godugu C, Patel A R, Desai U, Andey T, Sams A, Singh M and Jablons D 2013 AlgiMatrixTM based 3D cell culture system as an *in-vitro* tumor model for anticancer studies *PLoS One* **8** e53708

[26] Schuessler T K, Chan X Y, Chen H J, Ji K, Park K M, Roshan-Ghias A and Kuhn N Z 2014 Biomimetic tissue-engineered systems for advancing cancer research: NCI strategic workshop report *Cancer Research.* **74** 5359–63

[27] Kilic C, Girotti A, Rodriguez-Cabello J C and Hasirci V 2014 A collagen-based corneal stroma substitute with micro-designed architecture *Biomater. Sci.* **2** 318–29

[28] Komez A, Baran E T, Erdem U, Hasirci N and Hasirci V 2016 Construction of a patterned hydrogel–fibrous mat bilayer structure to mimic choroid and Bruch's membrane layers of retina *J. Biomed. Mater. Res.* A **104** 2166–77

[29] Drexler J W and Powell H M 2011 Dehydrothermal crosslinking of electrospun collagen *Tissue Eng.* C **17** 9–17

[30] Pang L, Hu Y, Yan Y, Liu L, Xiong Z, Wei Y and Bai J 2007 Surface modification of PLGA/β-TCP scaffold for bone tissue engineering: hybridization with collagen and apatite *Surf Coatings Technol.* **201** 9549–57

[31] Lin L and Gao H 2016 Modification of β-TCP/PLGA scaffold and its effect on bone regeneration *in vivo J Wuhan Univ Technol Sci Ed.* **31** 454–60

[32] Yang Y, Tang G, Zhao Y, Zhang Y, Li X and Yuan X 2011 Effect of degradation of PLGA and PLGA/β-TCP scaffolds on the growth of osteoblasts *Chinese Sci. Bull.* **56** 982–6

[33] Kim S H, Kim S H and Jung Y 2015 Bi-layered PLCL/(PLGA/β-TCP) composite scaffold for osteochondral tissue engineering *J. Bioact. Compat. Polym.* **30** 178–87

[34] Fitzgerald K A, Guo J, Tierney E G, Curtin C M, Malhotra M, Darcy R, O'Brien F J and O'Driscoll C M 2015 The use of collagen-based scaffolds to simulate prostate cancer bone metastases with potential for evaluating delivery of nanoparticulate gene therapeutics *Biomaterials* **66** 53–66

[35] Sheikh Z, Najeeb S, Khurshid Z, Verma V, Rashid H and Glogauer M 2015 Biodegradable materials for bone repair and tissue engineering applications *Materials* **8** 5744–94

[36] Jabbari E, Sarvestani S K, Daneshian L and Moeinzadeh S 2015 Optimum 3D matrix stiffness for maintenance of cancer stem cells is dependent on tissue origin of cancer cells *PLoS One* **10** e0132377

[37] He X, Kawazoe N and Chen G 2014 Preparation of cylinder-shaped porous sponges of poly(L-lactic acid), poly(DL-lactic-co-glycolic acid), and poly(ε-caprolactone) *Biomed Res. Int.* **2014** 1–8

[38] Iannace S, Maio E and Di Nicolais L 2001 Preparation and characterization of polyurethane porous membranes by particulate-leaching method *Cell. Polym.* **20** 321–38

[39] Lehocký M, Drnovská H, Lapčíková B, Barros-Timmons A, Trindade T, Zembala M and Lapčík L 2003 Plasma surface modification of polyethylene *Colloids and Surfaces* A **222** 125–31

[40] Cvelbar U, Mozetic M and Klanjsek-Gunde M 2005 Selective oxygen plasma etching of coatings *IEEE T. Plasma Sci.* **33** 236–7

[41] Nagahara S and Matsuda T 1996 Cell–substrate and cell–cell interactions differently regulate cytoskeletal and extracellular matrix protein gene expression *J. Biomed. Mater. Res.* **32** 677–86

[42] Gumbiner B M 1996 Cell adhesion: the molecular basis of tissue architecture and morphogenesis *Cell* **84** 345–57
[43] Ozcan C and Hasirci N 2007 Plasma modification of PMMA films: surface free energy and cell-attachment studies *J. Biomater. Sci. Polym. Ed.* **18** 759–73
[44] Hasirci V, Tezcaner A, Hasirci N and Süzer S 2003 Oxygen plasma modification of poly(3-hydroxybutyrate-co-3-hydroxyvalerate) film surfaces for tissue engineering purposes *J. Appl. Polym. Sci.* **87** 1285–9
[45] Vardar E, Endogan T, Kiziltay A, Hasirci V and Hasirci N 2010 Effect of oxygen plasma on surface properties and biocompatibility of PLGA films *Surf. Interface Anal.* **42** 486–91
[46] Lu L, Peter S J, Lyman M D, Lai H-L, Leite S M, Tamada J A, Uyama S, Vacanti J P, Langer R and Mikos A G 2000 *In vitro* and *in vivo* degradation of porous poly(dl-lactic-co-glycolic acid) foams *Biomaterials* **21** 1837–45
[47] Loh Q L and Choong C 2013 Three-dimensional scaffolds for tissue engineering applications: role of porosity and pore size *Tissue Eng.* B **19** 485–502
[48] Artel A, Mehdizadeh H, Chiu Y-C, Brey E M and Cinar A 2011 An agent-based model for the investigation of neovascularization within porous scaffolds *Tissue Eng.* A **17** 2133–41
[49] Pulieri E, Chiono V, Ciardelli G, Vozzi G, Ahluwalia A, Domenici C, Vozzi F and Giusti P 2008 Chitosan/gelatin blends for biomedical applications *J. Biomed. Mater. Res.* A **86** 311–22
[50] Goldbloom-Helzner L, Hao D and Wang A 2019 Developing regenerative treatments for developmental defects, injuries, and diseases using extracellular matrix collagen-targeting peptides *Int. J. Mol. Sci.* **20** 4072
[51] Edwards N, Langford-Smith A W W, Wilkinson F L and Alexander M Y 2018 Endothelial progenitor cells: new targets for therapeutics for inflammatory conditions with high cardiovascular risk *Front. Med.* **5** 200
[52] Intranuovo F, Howard D, White L J, Johal R K, Ghaemmaghami A M, Favia P, Howdle S M, Shakesheff K M and Alexander M R 2011 Uniform cell colonization of porous 3D scaffolds achieved using radial control of surface chemistry *Acta Biomater.* **7** 3336–44
[53] Chaddad H, Kuchler-Bopp S, Fuhrmann G, Gegout H, Ubeaud-Sequier G, Schwinté P, Bornert F, Benkirane-Jessel N and Idoux-Gillet Y 2017 Combining 2D angiogenesis and 3D osteosarcoma microtissues to improve vascularization *Exp. Cell. Res.* **360** 138–45
[54] Bachelder R E, Crago A, Chung J, Wendt M A, Shaw L M, Robinson G and Mercurio A M 2001 Vascular endothelial growth factor is an autocrine survival factor for neuropilin-expressing breast carcinoma cells *Cancer Res.* **61** 5736–40
[55] Deckers M M L, Karperien M, van der Bent C, Yamashita T, Papapoulos S E and Löwik C W 2000 Expression of vascular endothelial growth factors and their receptors during osteoblast differentiation *Endocrinology* **141** 1667–74
[56] Peng N, Gao S, Guo X, Wang G, Cheng C, Li M and Liu K 2016 Silencing of VEGF inhibits human osteosarcoma angiogenesis and promotes cell apoptosis via VEGF/PI3K/AKT signaling pathway *J. Transl. Res.* **8** 1005–15
[57] Coch L, Mejias M, Berzigotti A, Garcia-Pras E, Gallego J, Bosch J, Mendez R and Fernandez M 2014 Disruption of negative feedback loop between vasohibin-1 and vascular endothelial growth factor decreases portal pressure, angiogenesis, and fibrosis in cirrhotic rats *Hepatology* **60** 633–47
[58] Lobov I B, Renard R A, Papadopoulos N, Gale N W, Thurston G, Yancopoulos G D and Wiegand S J 2007 Delta-like ligand 4 (Dll4) is induced by VEGF as a negative regulator of angiogenic sprouting *Proc. Natl Acad. Sci.* **104** 3219–24
[59] Suzuki Y, Kobayashi M, Miyashita H, Ohta H, Sonoda H and Sato Y 2010 Isolation of a small vasohibin-binding protein (SVBP) and its role in vasohibin secretion *J. Cell Sci.* **123** 3094–101
[60] Saito T *et al* VEGF-A induces its negative regulator, soluble form of VEGFR-1, by modulating its alternative splicing *FEBS Lett.* 2013 **587** 2179–85
[61] Ning Y *et al* Interleukin-8 is associated with proliferation, migration, angiogenesis and chemosensitivity *in vitro* and *in vivo* in colon cancer cell line models *Int. J. Cancer.* 2011 **128** 2038–49
[62] Tan P H S, Chia S S, Toh S L, Goh J C H and Nathan S S 2014 The dominant role of IL-8 as an angiogenic driver in a three-dimensional physiological tumor construct for drug testing *Tissue Eng.* A **20** 1758–66
[63] Zanoni M, Piccinini F and Arienti C 2016 3D tumor spheroid models for *in vitro* therapeutic screening: a systematic approach to enhance the biological relevance of data obtained *Sci. Rep.* **6** 19103